Research Square

Preprints are preliminary reports that have not undergone peer review.
They should not be considered conclusive, used to inform clinical practice,
or referenced by the media as validated information.

Acoustic Based Wireless Power Transfer for Energy Delivery to Rotating Load Applications

Yusmarnita Yusop

yusmarnita@utem.edu.my

Universiti Teknikal Malaysia Melaka

Nurazreen Insyirah

Universiti Teknikal Malaysia Melaka

Cheok Yan Qi

Universiti Teknikal Malaysia Melaka

Huzaimah Husin

Universiti Teknikal Malaysia Melaka

Shakir Saat

Higher Colleges of Technology

Peter Adam Hoeher

Christian-Albrechts-Universität zu Kiel

Research Article

Keywords:

Posted Date: November 25th, 2026

DOI: https://doi.org/10.21203/rs.3.rs-10375614/v1

License: This work is licensed under a Creative Commons Attribution 4.0 International License.
Read Full License

Additional Declarations: No competing interests reported.

Acoustic Based Wireless Power Transfer for Energy Delivery to Rotating Load Applications

Yusmarnita Yusop[1], Nurazreen Insyirah[1] ,Cheok Yan Qi[1], , Huzaimah Husin[1], Shakir Saat[2], Peter Adam Hoeher[3]
[1]Centre of Telecommunication Research & Innovation, Faculty Technology of Electronic and Computer Engineering, Universiti Teknikal Malaysia Melaka, Melaka, Malaysia
[2]Faculty of Engineering Technology and Science, Higher Colleges of Technology, Abu Dhabi, United Arab Emirates
[3]Kiel University, Germany

***Abstract*— This project presents an acoustic wireless power transfer (AWPT) system for continuous contactless energy delivery to rotating loads. In conventional rotating electrical systems, power is commonly supplied through cables or slip rings. However, these approaches become unreliable when the load rotates beyond 360°, resulting in cable entanglement, twisting, mechanical wear, and increased maintenance requirements. Although electromagnetic wireless power transfer (WPT) eliminates physical contacts, its power transfer performance is highly sensitive to misalignment and dynamic rotational conditions. To overcome these limitations, this research proposes an AWPT system capable of delivering continuous electrical power to rotating loads without mechanical contact or cable constraints. The proposed system employs piezoelectric transducers as the acoustic energy coupling medium, driven by a high-efficiency Class-E resonant inverter integrated with an LCLC impedance matching network operating at 40 kHz. The research methodology comprises impedance characterisation of the piezoelectric transducers, comparative evaluation of power transfer performance under single-input single-output (SISO), single-input multiple-output (SIMO), multiple-input single-output (MISO), and multiple-input multiple-output (MIMO) configurations with both series and parallel interconnections, followed by hardware implementation and experimental validation using a motorised platform capable of continuous rotation beyond 360°. Experimental results demonstrate that the MIMO series–series (MIMO-SS) configuration achieves the highest power transfer stability and efficiency under rotational conditions and was therefore selected for the final prototype implementation. The developed AWPT prototype, powered by the Class-E LCLC inverter, achieved a maximum power transfer efficiency of 89.3% under resistive loading while providing stable excitation of the piezoelectric transducers. Continuous power delivery was successfully maintained throughout unrestricted rotational motion with only a modest reduction in efficiency compared with static operation. Overall, the proposed AWPT system successfully eliminates cable entanglement while providing efficient and reliable contactless power transfer for continuously rotating loads. The findings demonstrate the feasibility of AWPT as a promising low-power energy transfer solution for rotating electromechanical systems, particularly in applications requiring unlimited rotational motion.**

Keywords*— *Acoustic Wireless Power Transfer (AWPT), Class-E Resonant Inverter, Piezoelectric Transducer (PZT), Rotating Systems, Power Transfer Efficiency

I. INTRODUCTION

Wireless Power Transfer (WPT) is a modern technology energy transfer that transmits electrical power across medium with no physical or wire connection. WPT technology offers a promising solution that provide a safe, efficient and contactless energy transfer which has been widely utilized for variety of applications ranging from high-power electrical vehicles [1], low-powered biomedical implants [2-3] wireless monitoring [4] and sensor powering [5-6].

The conventional WPT system typically consist of three key components which is transmitter unit, power transmission medium and receiver unit as illustrated in Figure 1.

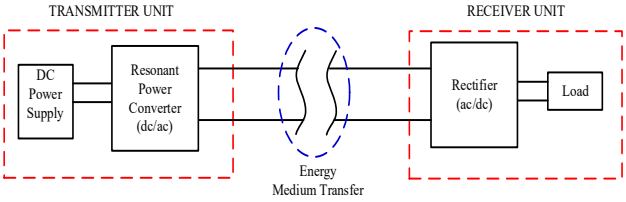

Figure 1. Block Diagram of Conventional WPT System

The transmitter powered by an external Direct Current (DC) power supply generates a time-varying electromagnetic field that act as an energy carrier. This field spreads across the medium to the receiver that captures the transmitted energy and then delivers it to the connected load or device. Despite their benefits and commercial success, WPT system approach face significant challenges in dynamic and harsh environments especially for rotating load application.

For conventional WPT approaches, they rely on slip rings or wired rotary joints. Slip rings introduces wear, friction and electrical noise [7]. Industries that uses slip ring or rotary joints to power robotic arms, machine tool spindles [8] and rotary sensors [9] suffers cable entanglement and weariness whereby making them unsuitable for long-term reliability.

Electromagnetic WPT system such as Inductive Wireless Power Transfer (IWPT) and Capacitive Wireless Power Transfer (CWPT) are among that mostly studied approach. IWPT utilizes near-field magnetic while CWPT require electric coupling. Both method aims in eliminating physical connectors to improve system reliability and enable energy. However, in [10], IWPT suffers from misalignment sensitivity and efficiency degradation due to reduced coupling while stray magnetic fields may introduce electromagnetic interference (EMI) concerns in practical implementations. In CWPT, precise plate alignment and dielectric-dependent air gaps limit the efficiency of coupling [11].

In contrast, Acoustic Wireless Power Transfer (AWPT) employs ultrasonic waves propagated through air, solids or fluids medium and is inherently immune to EMI making it a promising alternative for rotating environment. [12] studied

that an efficiency of 95.5% is able to be achieved with low-powered input. Conversely, AWPT for implantable devices prioritizes safety, exposure limits and minituarization over efficiency commonly remains below 10% [2]. H. Basaeri et al. [13] investigated that the efficiency of this propagation heavily depends on the acoustic impedance of the medium. Despite its advantages, AWPT performance depends heavily on the efficiency and robustness of their power electronic stage in converting DC input into high-frequency Alternating Current (AC) signals that drive the transmitting transducer. Most early AWPT implementations rely in linear amplifiers or hardswitching inverter which exhibit low efficiency and excessive thermal losses.

Among various power amplifier topologies, Class-E resonant inverter has emerged as one of the most widely used in WPT applications due to its high efficiency, soft switching characteristics and simple design. For high- frequency power transfer systems, LCLC compensation improves voltage magnification and allows operation under capacitive loads such as piezoelectric transducers [14]. While this approach has demonstrated efficiencies exceeding 85% in static WPT systems, its application to AWPT for rotating loads remain largely unexplored. Therefore, this research aims to design a high-efficiency Class-E resonant inverter circuit with impedance matching for driving piezoelectric transducer in AWPT systems under Multiple-Input-Multiple-Output-Series-Series (MIMO-SS) configuration to rotating loads.

The contribution of this paper can be explained as: (i) A compact AWPT architecture driven by a Class-E LCLC resonant inverter optimized for piezoelectric excitation and soft-switching operation at 40kHz. (ii) Implementation of MIMO-SS configuration for dynamic acoustic links. (iii) Experimental demonstration of slip-ring free AWPT for rotating loads. The hardware demonstration validate its continuous power transfer under rotation and record degradation of efficiency relative to static operation. (iv) Discussion of deployment implications that highlights how AWPT offers EMI immunity, reduced maintenance, and scalability for rotating applications.

II. Proposed AWPT System

A. Block Diagram of AWPT System

The overall system architecture of the proposed AWPT system is illustrated as in Figure 2.

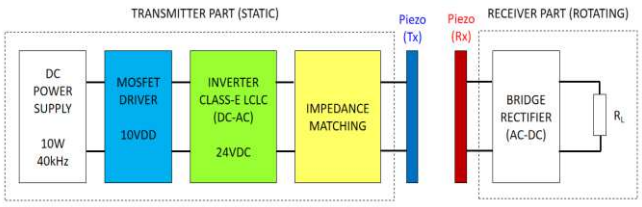

Figure 2. Proposed AWPT System Block Diagram for Rotating Load

The system comprises a stationary transmitter and a rotating receiver which are separated by acoustic piezoelectric device that transfers energy across an air gap via acoustic waves. Electrical energy from a 24 VDC source is first converted into high-frequency AC using a Class-E resonant inverter with an LCLC impedance matching network.

The AC excitation drives the transmitting piezoelectric transducer and generates ultrasonic waves that propagate through air and are subsequently captures by the receiver transducer. The received acoustic energy is converted back into electrical form, rectified and delivered to rotating load without any physical electrical contact. This configuration enables continuous power delivery while eliminating mechanical wear associated with slip rings or rotary joints.

B. Class-E LCLC Topology Design (Transmitter Part)

The design specification and circuit parameters of the Class -E LCLC circuit are summarized in Table 1. The component values are derived mathematically, following the methodology in [12], but recalculated based on new design specification tailored for AWPT system.

Table 1. Design Parameter

Symbol	Description	Values
Vdc	Voltage input for the Class-E inverter circuit	24V
Vdd	Supply input for MOSFET driver	10V
INPUT	Control input, TTL/CMOS compatible input for MOSFET driver where duty cycle is 50% and operating frequency is 40kHz	-
Vg	Gate voltage terminal	-
Vd	Drain voltage terminal	-
Vs	Source voltage terminal	-
Cs	Shunt Capacitor	22nf
Lf	Choke inductor	500uH
L	Resonant inductor	661uH
L2	Inductor L2	506uH
C2	Capacitor C2	21.56nf
C3	Capacitor C3	15.15nf
C4	Capacitor C4	38.64nf
RL	Load resistor for Class-E resonant inverter	50 Ω

Figure 3 shows the schematic of Class-E LCLC topology which combines a π1b matching circuit with LC matching components for transmitter compensation.

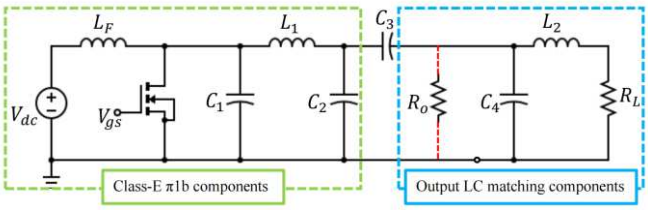

Figure 3. Class-E LCLC Circuit

The Class-E resonant inverter is selected due to its capability to achieve zero-voltage switching (ZVS), reducing switching losses and enabling high-frequency operation. The inverter operates at a supply voltage of $V_{DC} = 24$ V, duty cycle $D = 0.5$, and desired operating frequency $f = 40$ kHz. The output load is specified as $R_L = 50\ \Omega$ with a target power of $P_o = 10$ W. A design quality factor of $Q = 5$ is selected to shape the drain-voltage waveform for near-ideal Class-E ZVS operation. This inverter topology also implements a MOSFET power switch Vgs, a choke inductor Lf for constant DC current and an energy storage capacitor C1.

To minimize the switching loss, the π1b sub-network ensures zero-voltage switching (ZVS) at the transmitter by shaping the switch voltage waveform as in Figure 4 while the additional LC section comprising a parallel capacitor C_4 and a

series inductor L_2 provides impedance matching toward the receiving end.

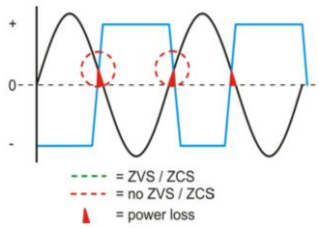

Figure 4. Zero Voltage Switching (ZVS) (Allan "Zardon" Campbell, 2015)

This dual LC configuration maintains ZVS operation and simultaneously reduces sensitivity to variations in load conditions. In this configuration, the actual load RL is retained equal to the capacitive reactance X_{C3} which enables π1b and LCLC sections to operate as a combined resonant structure. The added LC branch ensures that R_L=X_{C3} is presented to the resonant tank affecting the voltage increment across the intermediate load resistor Ro. The result is a practical L-C-L-C matching network that maximizes power transfer, preserves ZVS behaviour at transmitter side and improves overall system efficiency.

The implementation of the Class-E LCLC network at the transmitter side is essential in AWPT system. It ensures optimal impedance matching and resonant energy transfer into the piezoelectric load. The preservation of Zero-Voltage Switching (ZVS) and harmonic content suppression allows inverter to deliver a high-quality sinusoidal excitation to the transmitter. This directly improves the efficiency of acoustic conversion and reduction of thermal stress in the switching stage.

Next, simulation is performed using circuit simulation software such as MATLAB to analyse drain voltage waveform, switching current, output power and efficiency. Simulation results must satisfy three design criteria:

1. Drain voltage reaches zero before switch turn-on
2. Output waveform remains sinusoidal
3. Class E with PZT model efficiency more than 90%

If these conditions are not met, component values are adjusted iteratively until optimal performance is achieved. The experimental waveforms are compared with simulated results to verify agreement. If discrepancies are observed, component tolerances, parasitic elements, and impedance mismatches are analysed and corrected. Performance evaluation is conducted under resistive and transducer load to ensure stable operation under actual AWPT conditions.

C. *Piezoelectric Transducer Characteristics*

PZTs are widely used in AWPT system as it efficiently converts electrical energy into acoustic waves. Figure 5 indicates the series equivalent circuit of PZT which is also known as Butterworth Van-Dyke (BVD) model. It is the simplest models applicable for relatively high mechanical quality factor PZT where thermal dissipative elements in piezoeceramic could be neglected. PZTs behave as capacitive loads and are modeled using the BVD equivalent circuit, consisting of R_1, L_1, C_1 and C_p.

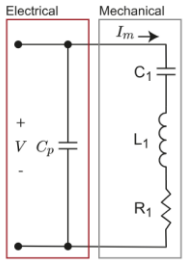

Figure 5. Series Equivalent Circuit of PZT (PiezoDrive, n. d.)

In this model, the electrical part represents the transducer capacitance while the mechanical part represents the mechanical response of the transducer. At the series resonance frequency, the reactance of C_1 and L_1 sum to zero which leaves only the resistance R_1. Therefore, at resonance, the total power delivered to the transducer can be evaluated using the following formula:

$$P = \frac{V_{rms}^2}{R_1} = I_{rms}^2 R_1 \tag{2.0}$$

However, the acoustic impedance between the piezoelectric ceramic and the air gap must be matched through acoustic matching layers to make the generated ultrasonic waves be transmitted efficiently. The impedance behavior of the BVD is represented using the complex impedance relationship as follows:

$$Z_T(\omega) = \frac{\left(\frac{1}{j\omega C_p}\right)\left(R_1 + j\omega L_1 + \frac{1}{j\omega C_1}\right)}{\left(\frac{1}{j\omega C_p}\right) + \left(R_1 + j\omega L_1 + \frac{1}{j\omega C_1}\right)} \tag{2.1}$$

where R represents the resistive component and ωL ωC represents the reactive component that varies with operating frequency. Thus, the performance of AWPT system depends strongly on how transmitters and receivers are arranged. Measurements for equivalent circuit parameters (R_1, L_1, C_1, C_p), quality factor (Q) and equivalent resistance (R) are conducted using an LCR meter across a frequency range surrounding the nominal operating frequency (40 kHz).

D. *Full-Wave Rectifier Design (Receiver Part)*

With validation on transmitter side, the subsequent stage focuses on the receiver subsystem where the electromechanical conversion characteristics of the selected PZT MIMO-SS configuration are examined for AWPT operation.

The receiver subsystem consists of characterised PZT that determines their electrical and electromechanical behaviour at the operating frequency of 40 kHz. Impedance measurements are performed to extract the resonance frequency, anti-resonance frequency and capacitive loading characteristics of the transducers in which influences the matching conditions and power transfer capability in the AWPT system. Then, the

AC output voltage from transducer receiver will be rectified into a pulsating DC using a full-wave rectifier composed of four diodes in a bridge arrangement as shown in Figure 6. Schottky diodes are preferred due to their low forward voltage drop and minimizes power losses at the load. The bridge design also eliminates the need for a center-tapped transformer, leading to a more compact and cost-effective circuit.

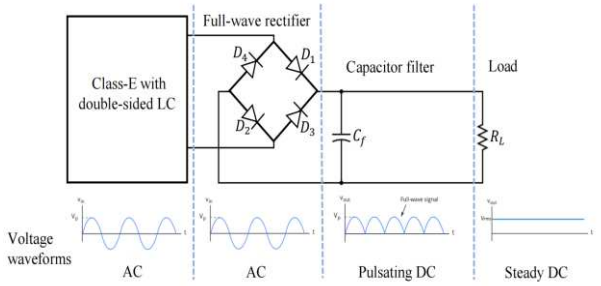

Figure 6. Block Diagram of Class-E LCLC with Full Wave Rectifier

A full-wave rectifier produces DC output voltage:

$$V_{dc} = \frac{2V_{peak}}{\pi} \tag{2.2}$$

Hence, the DC power delivered can be expressed as:

$$P_{dc} = \frac{V_{dc}^2}{R_L} \tag{2.3}$$

Equation (2.3) highlights that Pdc < Pac where the rectification introduces losses even under ideal assumptions. For transducer receiver configuration, the measurement of output voltage, current, and received power are taken using oscilloscope (DSO-X 2012A) and calibrated probes to evaluate the effectiveness of acoustic energy conversion. Load resistance is kept constant to ensure consistent comparison between configurations.

The electrical quantities are recorded under identical excitation conditions enabling a fair evaluation of how series and parallel interconnections influence impedance, voltage distribution as well as overall received power. This measurement procedure provides the basis for determining the efficiency of receiver configuration for subsequent system-level testing.

III. Piezoelectric Transducer Design

A. Piezoelectric Transducer Setup

The transducers are configured to enable non-contact energy coupling through medium (air). Figure 7 shows transmitter (Tx) and receiver (Rx) of air ultrasonic ceramic transducers used as PZT for the proposed AWPT system.



Figure 7. Air Ultrasonic Ceramic Transducer

Tx (400ST100) converts electrical excitation from the Class-E LCLC inverter into acoustic pressure waves and provides a sound pressure level of approximately 112 dB with a –6 dB bandwidth of 2.5 kHz. Rx (400SR100) converts the incoming acoustic waves back into electrical energy with a sensitivity of –70 dB and a capacitance of approximately 1900 pF. Both devices exhibit narrowband resonant behaviour at 40 kHz making them suitable for impedance matching and resonant energy coupling. The proposed AWPT system will utilise 10 PZT for both Tx and Rx under series interconnection as shown in Figure 8.

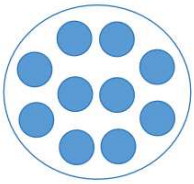

Figure 8. PZT Design Layout at both Tx and Rx

The PZT is positioned and designed in a circular shape to maximize piezo spatial coverage during rotating motion. Wire jumpers and adder pins are first soldered to PCB. Then, the components are tested and validated for signal continuity and minimal noise.

In AWPT system, the Tx will remain in a stationary position connected to Class-E LCLC circuit while the Rx is mounted on the rotating platform to allow continuous rotation without slip rings. This configuration enables efficient non-contact power transfer to rotating loads. Next, the subsequent stage will be focusing on the selected arrangement for PZT.

B. MIMO-SS Configuration

Figure 9 illustrates MIMO-SS arrangement selected and used to characterize the acoustic response of 10 Tx and 10 Rx. A waveform generator (DSO-X 2012A) from the oscilloscope combined with a waveform amplifier (TS250) supplies a sinusoidal excitation AC signal to the transmitter. After confirming the electrical connection of PZT MIMO-SS arrangement, the arrangement is integrated into the experimental setup illustrated in Figure 10.

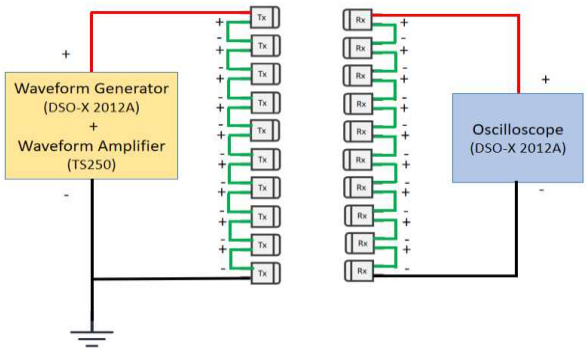

Figure 9. MIMO-SS Arrangement

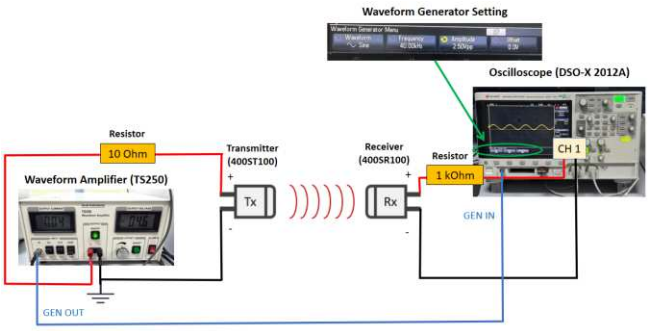

Figure 10. Experimental Setup for MIMO-SS Arrangement

The transmission efficiency is evaluated using a 40 kHz AC waveform with a 0.5 duty cycle, high-impedance (Hi-Z) output and 2.5 Vp-p voltage amplitude which is generated by the waveform function of oscilloscope. The signal is routed through waveform amplifier to supply piezoelectric Tx device where the signal is amplified with a gain of 20 dB resulting in an output of approximately 25 Vp-p. The maximum allowable drive voltage of PZT is specified to be 28 Vp-p per piezo. Therefore, it is important that the voltage across each transducer is monitored to ensure that its limit is not exceeded and the efficiency of transducer configuration is in safe condition for extended operation.

The output of PZT Rx unit is monitored and analysed using an oscilloscope to assess waveform integrity and energy transfer performance. The PZTs are tested in the range of 1cm to 30 cm. Key measurements included Vp-p, Ip-p, power input, power output and efficiency. For MIMO-SS mode, both series Tx and Rx are tested in 10 units respectively. The arrangement is examined by the behaviour of Tx and Rx enabling comparison of acoustic coupling performance, alignment sensitivity, and overall signal stability.

IV. RESULT AND DISCUSSION

A. Analysis of PZT MIMO-SS Configuration

The first phase focuses on investigating the power transfer characteristics and impedance behaviour of PZT under MIMO configuration with further evaluation of electrical interconnections of series-series (SS) mode. Figure 11 shows the experimental setup for PZT which is used to evaluate MIMO-PP interconnection across 1 cm to 30 cm. A 10 Ohm resistor is connected in series with piezo transmitter while 1 kOhm resistor is connected in series with piezo receiver to measure input and output current piezo with a current probe and ultimately evaluating input power, output power and efficiency of PWT.

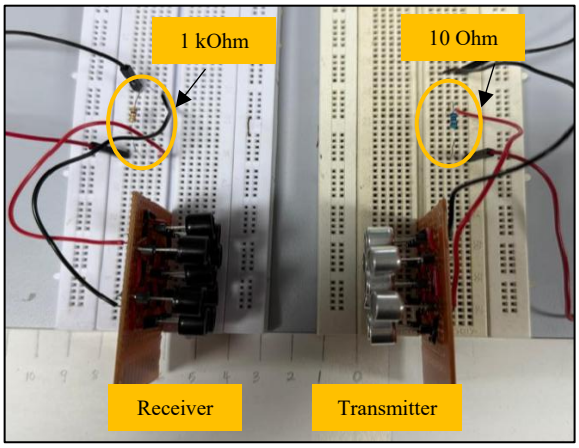

Figure 11. Experimental Setup of MIMO-SS

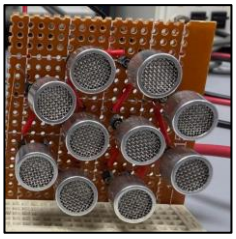

Figure 12. Series Wiring Connection of MIMO-SS

Figure 12 shows the PZT MIMO-SS arrangement and wiring connection is carried out as in Figure 9 using 40kHz excitation signal. The evaluation is determined based on output voltage stability, efficiency consistency and safe operating margins with respect to the piezoelectric voltage limit of 28Vp-p.

As in Figure 13, the outcome of MIMO-SS configuration shows a robust and stable performance across the medium gap (air) with a distance endurance from 6 cm up to 24 cm before it slightly drop till 30 cm. The series connection (SS) gives a smoother decay and improved impedance matching resulting from stable voltage and current behaviour without exceeding transducer limits.

The distributed transmitter-receiver array minimizes the localized impedance mismatches and provide spatial energy loss. This significantly reduces coupling sensitivity to minor alignment variations which particularly beneficial for rotating platforms as the coupling alignment continuously changes during operation.

Observing from an application standpoint, rotating loads introduces variable of air gaps, angular misalignments and vibration. Therefore, the configuration must maximize its spatial coupling while minimizing sensitivity to instant changes in geometry while rotating. Overall, the PZT MIMO-SS configuration consistently delivers an optimal and balanced performance in terms of efficiency stability, voltage compliance, impedance uniformity and distance tolerance.

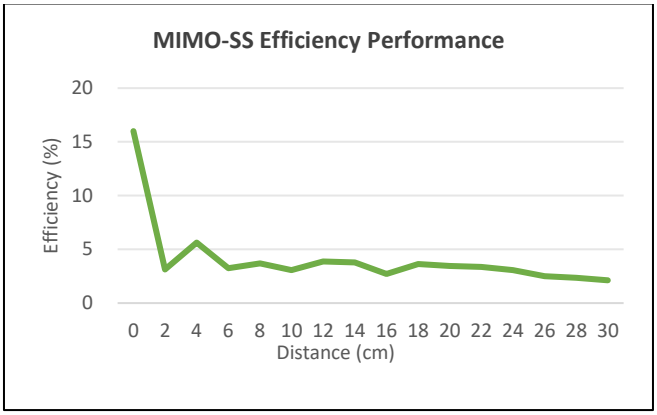

Figure 13. MIMO-SS Efficiency Performance

B. *Performance Analysis of Class-E LCLC Inverter*

The first analysis focuses on evaluating the switching performance of the Class-E LCLC inverter particularly the achievement of zero-voltage switching (ZVS) as well as the quality and magnitude of the voltage delivered to the load. The comparison of MOSFET switching behavior and output voltage–current waveforms obtained from MATLAB simulation and experimental measurements using both a resistive load and a piezoelectric load are analysed.

Referring to Figure 3, simulation circuit is designed using Simulink of MATLAB R2025b. In this designed circuit, the load applied is a non-inductive resistive load with a resistance of 50Ω and a power rating of 50 W, which is suitable for the target output power of 10 W. The simulation design parameters and the output performance of the Class-E LCLC matching network are presented in Table 2.

Subsequently, the switching voltage and efficiency performance for experimental setup in Figure 14 are analysed based on simulation validation.

Table 2. Design Parameter

Output Parameter		Results			
		Calculation	Simulation	Experiment (R_L)	Experiment (PZT_L)
V_{DC}	V	24	24	24.12	21.8
I_{DC}	A	0.42	0.43	0.40	0.46
V_{RL}	V	31.62	22.90	41	113
I_{RL}	A	0.63	0.46	0.21	0.14
P_{in}	W	10	10.30	9.6	10.0
P_{out}	W	10	9.50	8.6	1.8
η	%	100	92.23%	89.3%	18.00%

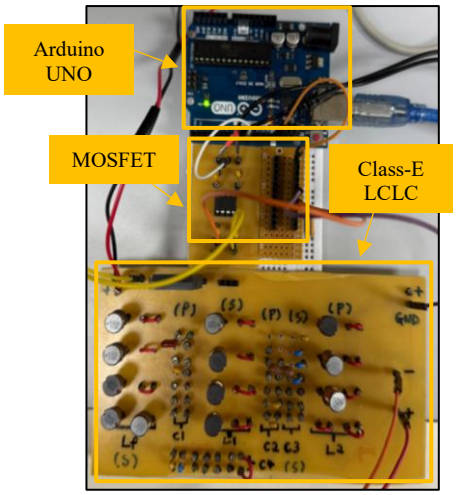

Figure 14. Circuit Setup for Class-E LCLC

All circuit parameters and design specification in Table 2 were calculated based on the derived equations. LCLC network was targeted to deliver 10 W output through a load resistor RL = 50 Ohm, which is higher than the optimum load value for Class-E operation. The research is considered successful if the Class-E LCLC inverter achieves at least 80% efficiency in the simulation.

From the simulation results in Table 2, the Vgs waveform remains stable at approximately 10 V, which is sufficient to fully enhance the MOSFET and ensure reliable switching operation. As in Figure 15(a), the corresponding drain-to-source voltage (Vds) waveform exhibits the characteristic quasi-sinusoidal waveform with a distinct zero-voltage switching (ZVS) condition at the turn-on instant. The peak voltage is observed to rise above the supply voltage consistent with ideal Class-E behaviour. This confirms that the zero-voltage switching is successfully achieved under simulated conditions.

The peak drain voltage reaches approximately 95.22 V which is around 3.96 times the DC input voltage of 24 V. This peak value is consistent with theoretical Class-E design expectations and validates the correctness of the LCLC impedance matching network in shaping the switch voltage waveform.

When transitioning from simulation to hardware implementation with a 50 Ω resistive load, the experimental performance remains at highly 89.3% of conversion efficiency. The result indicates that zero-voltage switching behaviour was preserved in practical conditions shown in Figure 15(b) while the LCLC matching network successfully minimizes switching losses. The general shape and switching behaviour correspond to the simulated case, albeit with minor deviation due to parasitic effects and non-ideal component behaviour. The experimental efficiency closely approaches the simulated value demonstrating Class-E LCLC network robustness under resistive loading.

By replacing the R_L with PZT_L, the experimental waveform shown in Figure 15(c) demonstrates increased distortion and capacitive loading characteristics when the R_L is replaced with PZT_L. This indicates that the inverter is effectively driving a reactive load consistent with the BVD piezoelectric model. Referring to Table 2, the voltage across the PZT_L experiences a higher peak voltage of 113 V but with lower current compared to the R_L case . This behaviour is

consistent with the capacitive nature of the PZT where voltage amplification occurs at resonance while current remains limited at 0.14 A. Consequently, the output power delivery of 1.8 W with lower measured efficiency of 18%. The reduction of power transfer efficiency is due to mechanical damping, acoustic radiation losses and impedance mismatch.

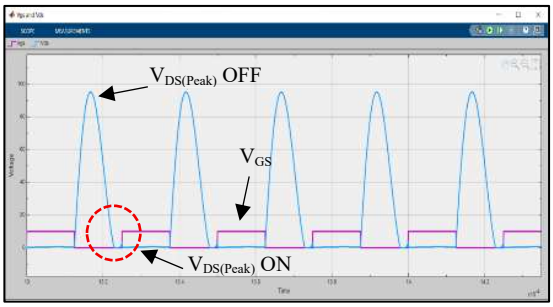

(a) MATLAB Simulation

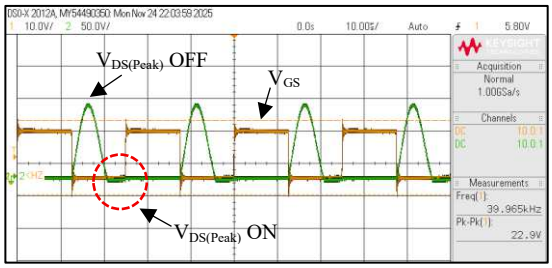

(b) R_L

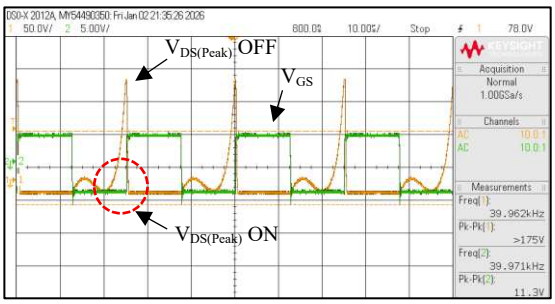

(c) PZT_L

Figure 15. ZVS Waveform

Next, the second analysis of the input voltage and current waveforms further highlights the differences between ideal and practical Class-E operation. The simulated input voltage and current waveforms shown in Figure 16(a) indicates that the Class-E LCLC inverter draws a steady DC input current from the supply while maintaining a constant input voltage level. The simulated current waveform exhibits low ripple due to the action of the choke inductor confirming that the analytical assumption of quasi-DC input current is satisfied.

Under experimental validation using a R_L (50 Ω) as shown in Figure 16(b), the measured input current exhibits a slightly higher ripple due to parasitic elements and measurement limitations. When the PZT_L is connected, the measured input current in Figure 16(c) shows additional variations arise from capacitive loading and reactive power flow.

However, the input voltage remains stable indicating that the transmitter can reliably supply the piezoelectric receiver under practical loading conditions. This behaviour aligns with the efficiency and power measurements where electrical output power decreases substantially when delivering acoustic energy to the piezoelectric receiver. The measured input voltage and current are used to compute input power directly.

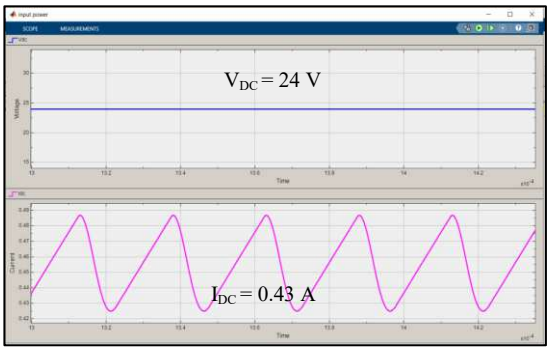

(a) MATLAB Simulation

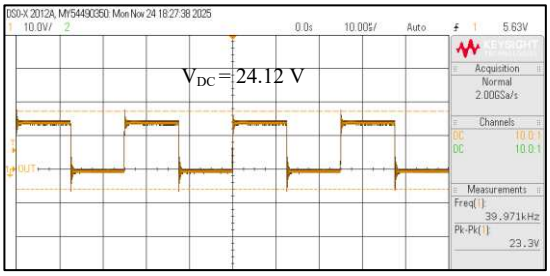

(b) R_L

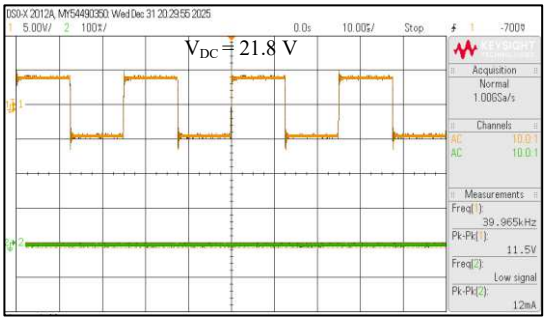

(c) PZT_L

Figure 16. Input Voltage and Current Waveform

Lastly, the comparison analysis of the voltage across the load between MATLAB simulation and experimental measurements reveals several key differences in waveform shape, amplitude and spectral content to compute the output power.

The simulated load voltage waveform is presented in Figure 17(a) where the output at 40 kHz remains sinusoidal with minimal harmonic distortion confirming the correct resonant operation.

Under experimental testing with a 50 Ω resistive load, Figure 17(b) shows that the measured waveform closely matches the simulated result in both frequency and waveform shape validating the impedance matching and resonant behaviour predicted by the analytical design.

When the PZT is connected, the measured waveform in Figure 17(c) shows higher voltage magnitude and additional reactive behaviour due to capacitive loading. This confirms that the inverter provides a sufficient excitation for the transducer and supports the acoustic energy transfer mechanism.

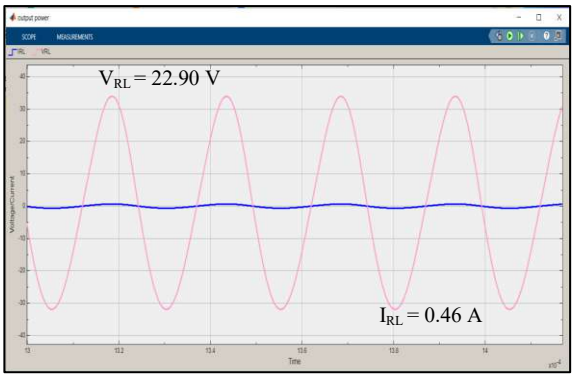

(a) MATLAB Simulation

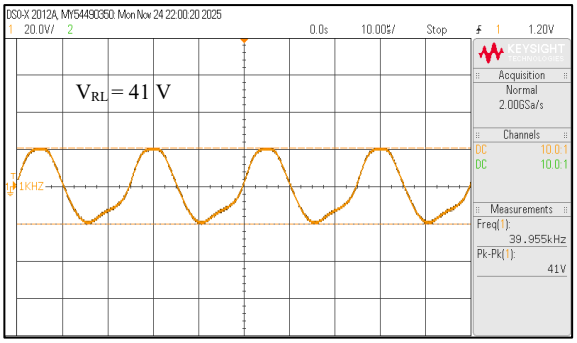

(b) R_L

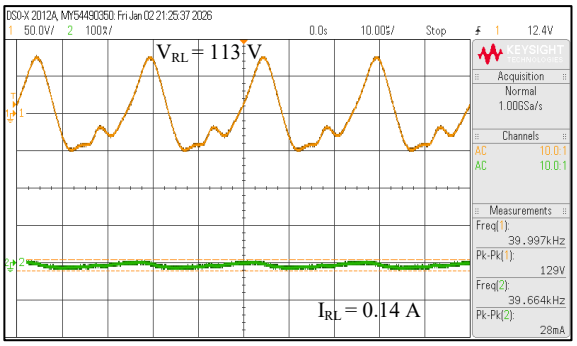

(c) PZT_L

Figure 17. Output Voltage and Current Waveform

The overall results confirm that the Class-E LCLC inverter have successfully achieve soft-switching behavior under both simulated and experimental conditions. While ideal ZVS and high efficiency performance are demonstrated in simulation, the experimental results highlight the impact of real-world losses and load non-linearity especially when driving the PZTs. Nevertheless, the preservation of near-ZVS operation and stable output waveforms demonstrates the robustness of the proposed inverter design and its suitability for AWPT applications.

C. Analysis of Rotating Load Performance

The complete experimental setup for rotating load evaluation is as shown in Figure 18 along with PZT setup in MIMO-SS configuration shown in Figure 19 for both transmitter and receiver.

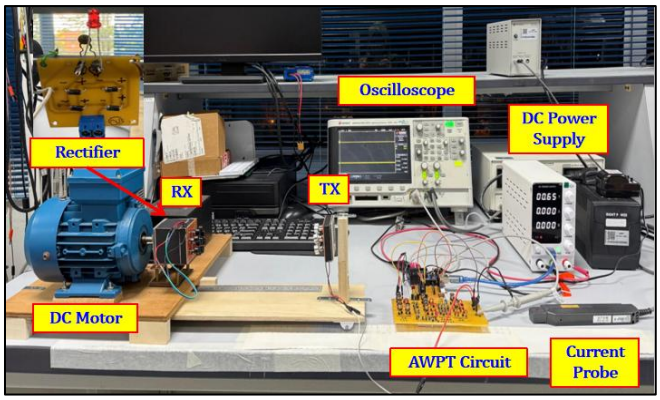

Figure 18. Full Setup of AWPT System

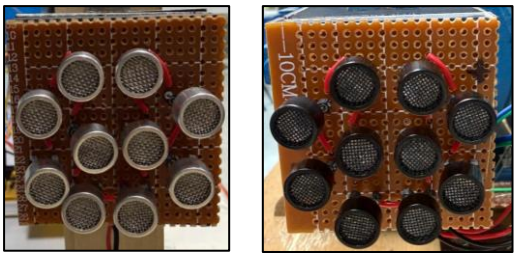

(a) PZT Transmitter (b) PZT Receiver

Figure 19. PZT Setup with Series Interconnection

The system integrates the Class-E LCLC resonant inverter developed with MIMO-SS PZT configuration. In the setup, the transmitter piezoelectric array remains fixed in a stationary position, while the receiver array is mounted on a motor-driven platform to enable continuous rotation. A DC motor provides the rotational motion, and its speed is manually adjusted to mimic realistic operating conditions found in rotating machinery.

During operation, acoustic energy generated by the transmitter propagates through air and is received by the rotating piezoelectric array, where it is converted back into electrical power. The recovered energy is rectified and used to drive a light-emitting diode (LED), which serves both as the load and as a visual indicator of continuous power transfer. This arrangement demonstrates effective wireless energy delivery to a rotating system without the need for slip rings or direct electrical contact.

Figures 20 shows a comparison of efficiency performance under static and rotating condition. In static condition, the system maintains relatively stable efficiency when the transmitter and receiver are closely aligned from 1 cm gap. The MIMO-SS configuration sustains relatively high and stable efficiency due to improved spatial coverage and distributed acoustic coupling across multiple transducers.

The series–series interconnection also helps maintain sufficient voltage levels for rectification while balancing voltage stress across the array. However, the efficiency gradually decreases as the separation distance increases up to 30 cm. The efficiency degradation becomes more pronounced with the combined influence of acoustic attenuation, impedance mismatch and reduced electromechanical conversion efficiency. This behaviour is consistent with the power–voltage-squared relationship where the efficiency degradation accelerates as the received voltage decreases, irrespective of whether the receiver is static or rotating.

Compared to the static condition, a slight reduction in rotating efficiency performance is observed across all tested distances. This drop is mainly attributed to rotation-induced effects such as minor misalignment, variations in acoustic coupling, and dynamic mechanical disturbances during motion.

One contributing factor of the efficiency drop is that mechanical rotation introduces small but continuous variations in the air gap between the transmitter and receiver. Even slight changes in this distance can noticeably affect acoustic coupling as ultrasonic transmission through air is highly sensitive to propagation distance. In addition, angular misalignment during rotation alters the effective acoustic radiation pattern which produces a time-varying coupling efficiency. Mechanical vibration and structural resonance from the rotating platform also contribute to additional losses that do not appear under static conditions.

Despite these dynamic disturbances, the proposed AWPT system can maintain continuous power delivery throughout rotation. The LED load remains illuminated without flickering. This indicates that the system operates reliably under motion. The observed reduction in efficiency during rotation remains within an acceptable margin where the acoustic coupling is intrinsically demonstrate more tolerant to rotational motion than inductive or capacitive WPT systems where they also typically experience severe performance degradation under misalignment.

These results indicate that system optimization should focus on improving acoustic impedance matching, maintaining resonant frequency stability, and refining transducer configurations rather than solely mitigating mechanical effects.

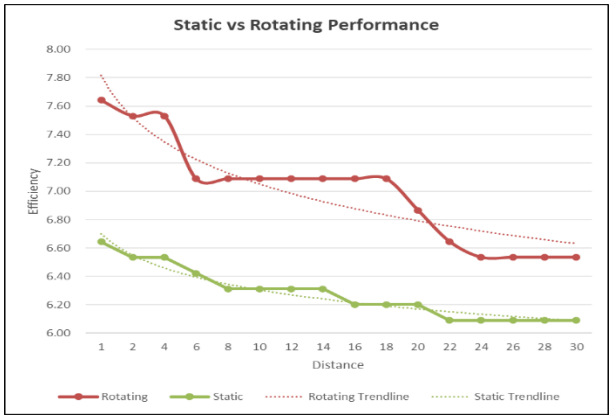

Figure 20. Static Vs Rotating Performance

V. Conclusion

This work presented the design and experimental validation of proposed AWPT system, with emphasis on achieving efficient and stable power delivery under practical operating conditions. Based on Class-E LCLC topology and PZT coupling mechanism, the proposed AWPT system was successfully analysed through both simulation and hardware implementation.

The obtained results demonstrate that the system can deliver consistent power with satisfactory efficiency. Under controlled conditions, the system achieved a maximum efficiency of approximately 92.23% in simulation, while the experimental setup recorded an efficiency of 89.30%, delivering an output power of 8.6 W. The difference between simulation and experimental results is mainly attributed to practical non-idealities such as switching losses, parasitic resistances, and component limitations. Despite these factors, the system maintained stable operation and reliable power transfer performance.

Furthermore, the analysis shows that system efficiency decreases as the transmission distance or misalignment increases due to the reduction in coupling strength. However, within the intended operating range, the AWPT system can sustain effective power transfer which demonstrate its robustness for real-world applications. The results also confirm that the Class-E LCLC topology provides good impedance matching and supports efficient energy conversion under varying load conditions.

Overall, the findings validate the feasibility of the proposed AWPT system as a practical wireless power transfer solution. Future improvements will focus on enhancing system efficiency and adaptability through advanced impedance tuning and improved coupling design. These enhancements are expected to further optimize performance and enable wider application of the system in dynamic and constrained environments.

References

[1] H. F. Leung and A. P. Hu, “Modeling and analysis of ultrasonic power transfer system with tightly coupled solid medium,” Wireless Power Transfer, vol. 4, no. 1, pp. 1–12, 2017.

[2] Z. Rong, M. Zhang, Y. Ning, and W. Pang, “An ultrasound-induced wireless power supply based on AlN piezoelectric micromachined ultrasonic transducers,” *Scientific Reports*, vol. 12, Art. no. 16174, Sep. 2022, doi: 10.1038/s41598-022-19693-5.

[3] C. Chen et al., “Micro triboelectric ultrasonic device for acoustic energy transfer and signal communication,” Nature Communications, vol. 11, no. 4143, 2020.

[4] Y. Li, J. Cui, G. Li, L. Liu, Y. Zheng, J. Zang, and C. Xue, “An Optimal Design Method for Improving the Efficiency of Ultrasonic Wireless Power Transmission during Communication,” Sensors, vol. 22, no. 3, p. 727, Jan. 2022.

[5] F.-G. Tseng, S. S. Bedair, and N. Lazarus, “Acoustic wireless power transfer with receiver array for enhanced performance,” *IEEE Transactions on Ultrasonics, Ferroelectrics, and Frequency Control*, vol. 64, no. 6, pp. 918–927, Jun. 2017.

[6] H. Yang, M. Wu, Z. Yu, and J. Yang, “An Ultrasonic Through-Metal-Wall Power Transfer System with Regulated DC Output,” Applied Sciences, vol. 8, no. 5, p. 692, 2018.

[7] J. Wang, Y. Li, and H. Zhang, “Reliability analysis of slip rings in rotating electrical machinery,” IEEE Transactions on Industry Applications, vol. 56, no. 4, pp. 3892–3901, Jul.–Aug. 2020.

[8] V. Kindl, T. Kavalir, J. Sika, J. Hnatik, M. Krizek, and M. Frivaldsky, “Wireless power transmission system for powering rotating parts of automatic machineries,” *Energies*, vol. 15, no. 18, p. 6856, Sept. 2022, doi: 10.3390/en15186856.

[9] V. A. Hoang and Y. C. Lee, “Capacitive-wireless power transfer system for power supply of a wireless sensor system on a propulsion shaft,” *Progress In Electromagnetics Research Letters*, vol. 102, pp. 9–18, 2022.

[10] C. Y. Liu, G. B. Wang, C. C. Wu, E. Y. Chang, S. Cheng, and W. H. Chieng, “Derivation of the resonance mechanism for wireless power

transfer using Class-E amplifier," *Energies*, vol. 14, no. 3, 2021, Art. no. 632, doi: 10.3390/en14030632.

[11] Y. Yusop, M. A. M. Radzi, and Z. Z. Abidin, "Analysis of misalignment effects in wireless power transfer systems," IEEE Transactions on Industrial Electronics, vol. 66, no. 6, pp. 4571–4580, Jun. 2019.

[12] H. Husin, S. Saat, Y. Yusop, A. Awang Md Isa, S. Mohd Isa, M. Darsono, A. Yahya, and S. K. Nguang, "Class E ZVS inverter simulation for series resonance mode ultrasonic transducer," *Journal of Telecommunication, Electronic and Computer Engineering*, vol. 9, no. 4, pp. 91–96, 2017.

[13] H. Basaeri, Y. Yu, D. Young, and S. Roundy, "Acoustic power transfer for biomedical implants using piezoelectric receivers: Effects of misalignment and misorientation," *Journal of Micromechanics and Microengineering*, vol. 29, no. 8, p. 084004, Jun. 2019, doi: 10.1088/1361-6439/ab257f.

[14] M. Venkatesan *et al*., "A review of compensation topologies and control techniques of bidirectional wireless power transfer systems for electric vehicle applications," *Energies*, vol. 15, no. 20, 2022, doi: 10.3390/en15207816.

[15] Allan "Zardon" Campbell, 2015, *be quiet! Dark Power Pro 11 550W Review* | KitaGuru-Part 4 [Online]. Available at: https://www.kitguru.net/components/power-supplies/zardon/be-quiet-dark-power-pro-11-550w-review/4/ (Accessed: *13 August 2025*).

[16] PiezoDrive, n.d. *Introduction to Ultrasonic Drivers*. Available at: https://www.piezodrive.com/ultrasonic-drivers/intro-ultrasonic/?srsltid=AfmBOopjG4GDo80QKPSR0CyBRIoUoY5GrzVPrO8s9RN9jolEHl_Zz0Cu (Accessed: *13 August 2025*).